12-1-2015

Digital tomosynthesis and high resolution computed tomography as clinical tools for vertebral endplate topography measurements: Comparison with microcomputed tomography.

Daniel Oravec
Henry Ford Health System, DORAVEC1@hfhs.org

Abrar Quazi
Henry Ford Health System

Angela Xiao
Henry Ford Health System

Ellen Yang
Henry Ford Health System

Roger Zauel
Henry Ford Health System, RZAUEL1@hfhs.org

See next page for additional authors

Recommended Citation

Oravec D, Quazi A, Xiao A, Yang E, Zauel R, Flynn MJ, and Yeni YN. Digital tomosynthesis and high resolution computed tomography as clinical tools for vertebral endplate topography measurements: Comparison with microcomputed tomography. Bone 2015; 81:300-305

Authors
Daniel Oravec, Abrar Quazi, Angela Xiao, Ellen Yang, Roger Zauel, Michael J. Flynn, and Yener N. Yeni

Bone 81 (2015) 300–305

Contents lists available at ScienceDirect

Bone

journal homepage: www.elsevier.com/locate/bone

Original Full Length Article

Digital tomosynthesis and high resolution computed tomography as clinical tools for vertebral endplate topography measurements: Comparison with microcomputed tomography

Daniel Oravec [a], Abrar Quazi [a], Angela Xiao [a], Ellen Yang [a], Roger Zauel [a], Michael J. Flynn [b], Yener N. Yeni [a,*]

[a] Bone and Joint Center, Henry Ford Hospital, Detroit, MI, United States
[b] Department of Radiology, Henry Ford Hospital, Detroit, MI, United States

ARTICLE INFO

Article history:
Received 17 February 2015
Revised 7 July 2015
Accepted 24 July 2015
Available online 26 July 2015

Keywords:
Vertebral bodies
Endplate topography
Digital tomosynthesis
Microcomputed tomography
Computed tomography

ABSTRACT

Endplate morphology is understood to play an important role in the mechanical behavior of vertebral bone as well as degenerative processes in spinal tissues; however, the utility of clinical imaging modalities in assessment of the vertebral endplate has been limited. The objective of this study was to evaluate the ability of two clinical imaging modalities (digital tomosynthesis, DTS; high resolution computed tomography, HRCT) to assess endplate topography by correlating the measurements to a microcomputed tomography (μCT) standard. DTS, HRCT, and μCT images of 117 cadaveric thoracolumbar vertebrae (T10–L1; 23 male, 19 female; ages 36–100 years) were segmented, and inferior and superior endplate surface topographical distribution parameters were calculated. Both DTS and HRCT showed statistically significant correlations with μCT approaching a moderate level of correlation at the superior endplate for all measured parameters ($R^2_{Adj} = 0.19–0.57$), including averages, variability, and higher order statistical moments. Correlation of average depths at the inferior endplate was comparable to the superior case for both DTS and HRCT ($R^2_{Adj} = 0.14–0.51$), while correlations became weak or non-significant for higher moments of the topography distribution. DTS was able to capture variations in the endplate topography to a slightly better extent than HRCT, and taken together with the higher speed and lower radiation cost of DTS than HRCT, DTS appears preferable for endplate measurements.

1. Introduction

Morphological features of human vertebral body endplates have been shown to be associated with important determinants of bone fragility and degenerative diseases of the spine. For instance, endplate thickness, curvature, and statistical moments of endplate topography distributions have been shown to be associated with vertebral load magnitude and distribution, microstructural properties of the underlying trabecular bone, vertebral failure strain and energy and intervertebral disc degeneration [1–6]. Microcomputed tomography (μCT) is typically used in such studies to produce a high resolution 3-dimensional depiction of vertebral endplate microarchitecture. However, μCT is only suitable in a laboratory setting with in vitro specimens due to size limitations and high radiation dose. Measurement of endplate topography using clinically available imaging modalities could improve assessment of vertebral bone quality in a clinical setting. To date, assessment of vertebral endplate using clinical imaging modalities has been limited to measurements such as density, thickness, and gross shape patterns [7–10].

Tomosynthesis was developed as a method to avoid superposition of objects present in conventional radiographic imaging and has evolved since its conception in the 1930s [11] through film [12] and fluoroscopy [13,14] techniques. Advances in flat panel digital detectors have realized a technology called digital tomosynthesis (DTS) [15]. Digital tomosynthesis is a tomographic imaging modality in which a series of projection images are acquired over a limited arc, with the X-ray source pivoting and translating opposite the direction of a flat panel detector encased in the scanning bed. Musculoskeletal DTS delivers 1/5th the dose or less than that of CT [16–18]. Tomosynthesis reconstructions of the spine are formed in the sagittal or coronal planes, in contrast with CT which produces an axial image with high slice thickness along the superior–inferior direction. Topographic features of the endplate surface are thus captured in-plane with a resolution of approximately 0.24 mm in DTS, rather than the axial resolution of 0.9 mm for HRCT; however, the out of plane slice sensitivity in DTS is about 3 mm [17,19]. Taken together, these features suggest that tomosynthesis might be a preferred clinical imaging modality for geometric analysis of the vertebral endplate.

The current study aims to correlate comparable measures of endplate topography between μCT, digital tomosynthesis (DTS) and high resolution computed tomography (HRCT) in order to assess the viability of endplate topography measurement in a clinical imaging modality.

* Corresponding author at: HFHS/IBio, Attn.: Bone & Joint Center, 6135 Woodward, Detroit, MI 48202, United States.

http://dx.doi.org/10.1016/j.bone.2015.07.033
8756-3282/

2. Methods

Human cadaveric thoraco-lumbar spines were acquired under local IRB approval from tissue banks and four vertebral bodies (T10, T11, T12, L1) were harvested from 42 donors. Donors with a history of HIV, hepatitis, diabetes, renal failure, metastatic cancer, osteomalacia, hyperparathyroidism, Paget's disease of bone, spine surgery, cause of death involving trauma, and corticosteroid, anticonvulsant or bisphosphonate use were not included. Vertebral bodies were dissected, soft tissue and posterior elements were removed, and specimens were stored wrapped in saline-soaked gauze at −20 °C until scanning was performed. The donor set consisted of 23 men and 19 women all between the ages of 36 and 100 years. Collectively, the vertebrae of these donors formed a set of 117 bones.

Specimens were mounted and consistently aligned in a custom radiolucent scanning tank filled with 0.9% saline and scanned using DTS (Shimadzu Sonialvision Safire II) and high resolution CT (Siemens Sensation 64). Scanning in saline-filled Lucite tanks (14 × 14 × 40 cm) was performed so as to establish bone–water contrast similar to the bone–tissue contrast encountered in vivo. Consistent endplate alignment was ensured using a radiolucent clamping system such that the anterior–posterior (AP) and lateral–medial (LM) anatomical directions were aligned to the reconstructed CT image axes. Tomosynthesis scans were performed in two orientations: AP (series of coronal slices) and LM (series of sagittal slices). The same specimens were scanned using a custom-built μCT system and reconstructed at an isotropic voxel size of 40 μm. The μCT system used in the study was based on the hardware, data acquisition, and reconstruction methods of the μCT system that has been previously described [20]. The presently operating system uses a Kevex 16-Watt X-ray source with a 9-micron focal spot, a 1888 × 1408-pixel Varian PaxScan 2520 flat panel digital X-ray detector with 127-micron pitch, a Newport precision rotational stage, and control software running under Windows XP.

For HRCT images, a single, unique threshold value in Hounsfield Units was manually determined for each vertebra as the minimum value that delineates bone from soft tissue. The threshold value was used within a custom segmentation algorithm to produce a closed surface gray value mask of the vertebral body [21], from which volume masks separating cortical and cancellous bone were segmented using a previously-described semi-automatic method [22]. The segmentation algorithm consists of dilating the binarized vertebral image twice (closing porosity within and on the surface of the vertebra), applying a median filter (connecting surfaces and smoothing processing artifacts), and eroding back twice. The resulting volume, a solid mask image of the whole vertebral body, was further cropped into separate volumes representing superior and inferior endplates. The topography of each endplate was assessed by creating a 2D height map in which each pixel represented the depth from a fixed plane (the first slice) to the first encounter of bone along the superior–inferior axis using the TopoJ plugin for ImageJ (Fig. 1) [23]. The depth distribution (background and holes were eliminated from the analysis) was recorded into a text file in which each row represented a single pixel in 2D height map. The average (Av), standard deviation, skewness (Skew), and kurtosis (Kurt) of the depth measurements were calculated to represent up to the fourth moment of the topography distribution [24]. A high average depth may represent the presence of large surface concavity or many deep pits, while standard deviation of the endplate topography distribution is a measure of endplate surface overall depth variation. Low average and standard deviation of depth are characteristic of a smooth surface. Skewness measures the symmetry of the depth distribution, and may be used as a measure of surface spikiness. Kurtosis measures the spread of the depth distribution (distribution sharpness may be influenced by features such as steep epiphyseal ring or a small number of steep peaks or valleys on the endplate surface). Kurtosis and skewness are understood to affect surface pressure distributions in engineering materials, such that high values of each result in high load bearing ratio and maximum contact pressure [25]. For instance, the combination of high kurtosis and low skewness has been shown to reduce friction [26].

A similar process was performed for DTS images. A global threshold value was manually determined to delineate bone from soft tissue and air. Due to a blurring effect in the highest and lowest slices of the DTS reconstructions, a central substack of 25 slices (25 mm) was created and the image was binarized in ImageJ using the recorded threshold value (Fig. 2a). Binarized images were cropped into separate volumes representing superior and inferior endplates. Depth distributions were again calculated for DTS endplate images and distribution statistics were calculated from DTS depth measurements. Additionally, depth

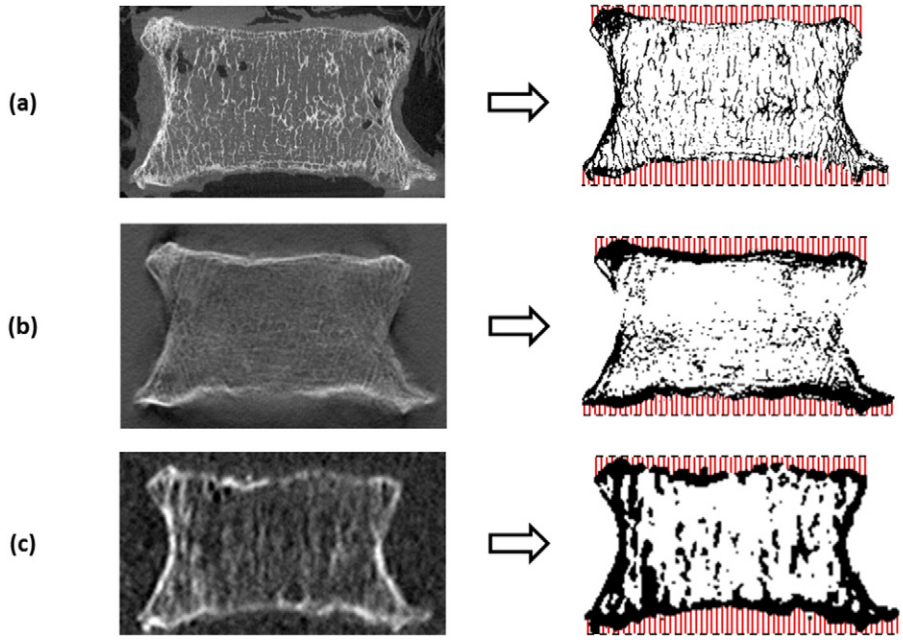

Fig. 1. Images were thresholded and depth distributions calculated from a fixed plane (dashed lines) at the superior and inferior endplates. Comparison of images taken from sagittal plane in similar regions from (a) μCT, (b) DTS (AP), and (c) HRCT. Images are resized to show detail at comparable scale.

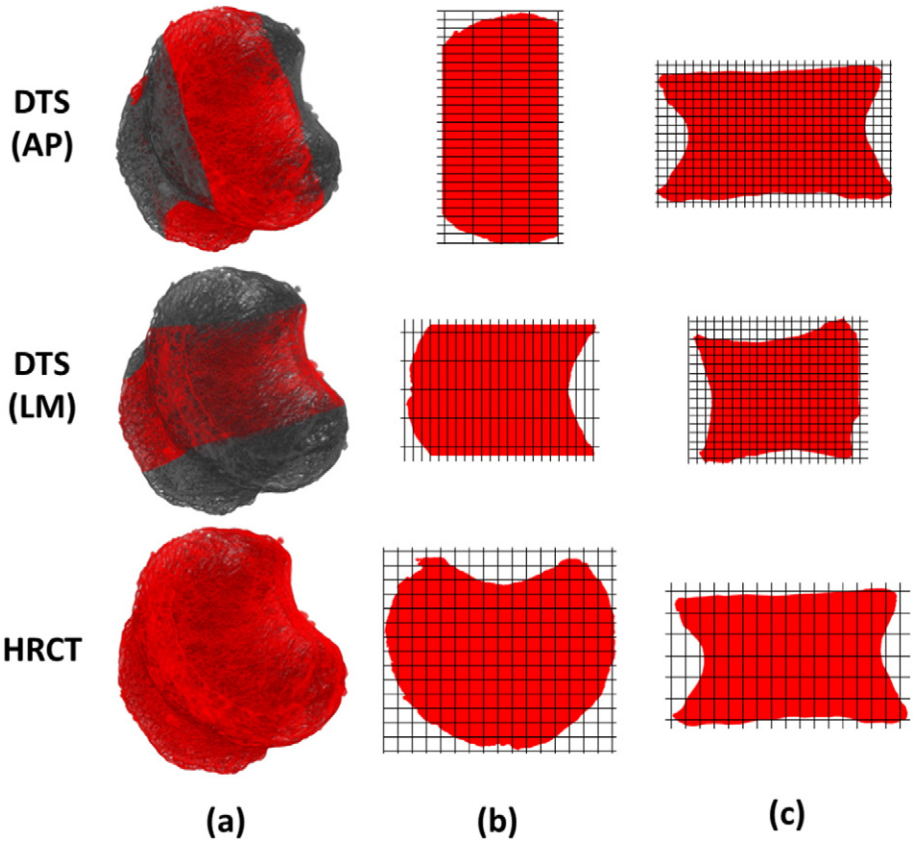

Fig. 2. (a) The analysis volume was prescribed as a 25 mm central slab in AP and LM DTS images to avoid blurring artifact, while HRCT VOI included the entire volume. Thus, the entire endplate was sampled for HRCT while a portion of the endplate was used in the DTS analysis. The portion of the endplate included in the DTS analysis depended on the view. (b) Note that pixel size is anisotropic in axial DTS images while it is isotropic in axial HRCT images. Within the volume included in the analysis, the quantity and spacing of sample points available for analysis are better in sagittal planes but poorer in coronal planes for AP DTS than for HRCT. In contrast, the quantity and spacing of sample points available for analysis are better in coronal planes but poorer in sagittal planes for LM DTS than for HRCT. (c) Pixel size is anisotropic in the measurement plane for HRCT images (with measurement resolution corresponding to slice thickness) and isotropic (coronal for AP, sagittal for LM) for DTS. DTS has superior sampling resolution along the axes perpendicular/parallel to the scanning direction, providing DTS considerably higher measurement resolution than HRCT within each plane of analysis. Note that grid lines demonstrate relative pixel spacing in DTS vs. HRCT and are not drawn to scale; figure prepared from μCT images for clarity.

frequencies were concatenated prior to calculating distribution statistics in order to create a pooled variable, representing a composite of the two DTS scanning directions.

Threshold values for μCT reconstructions were calculated from a $300 \times 300 \times 300$ voxel central cube of cancellous bone using the Otsu method in ImageJ and the whole image was binarized using this global threshold value. A custom algorithm was used to produce a depth frequency distribution representing distances from the superior-most and inferior-most reference planes to the inner surfaces of the vertebral endplate [6]. The custom algorithm used an approach similar to that of TopoJ but additional procedures were used to account for small voids present on the vertebral endplate in high resolution μCT images. In this method, surface voxels were compared to the surrounding neighborhood of voxels such that if a surface voxel is deeper than the mean plus 0.5 standard deviation of its neighborhood, the surface voxel was considered to be part of an open hole. Interpolating depths for open holes as the reciprocal-distance-squared weighted average of the neighborhood ensured a contiguous endplate surface. Distribution statistics were again calculated using the depth frequency distribution produced by this method for μCT.

For statistical analyses, the main interest was in the relationship between similar measurements from the μCT and DTS images and between those from the μCT and high resolution CT (HRCT) images. The relationships between μCT and DTS/HRCT variables were examined using mixed regression models with μCT variable as the outcome and the corresponding DTS or HRCT variable as the effect variable. The model included a random subject variable to account for pseudoreplication due to using multiple vertebral levels from some subjects. In order to gain further insight into the nature of examined relationships, differences in mean of statistical distribution parameters between superior and inferior endplates were examined for μCT images using paired t-tests. All analyses were performed in JMP (Version 7.0, SAS Institute Inc., Cary, NC).

In an effort to understand the feasibility of endplate topography measurements in clinical DTS images, two vertebral levels (T12, L1) were assessed from a single in vivo thoracolumbar spine DTS image using the same methods presented above for comparison with average outcome measures from the 117 in vitro specimens (Fig. 4). DTS scans of the patient (87Y male) were performed under IRB approval in the context of a metabolic survey for multiple myeloma.

3. Results

For the superior endplate, except for kurtosis calculated from pooled AP and LM DTS images, all DTS and HRCT measurements were significantly associated with the corresponding μCT measurements (Table 1). Calculations from μCT had stronger associations with those from AP DTS than with LM DTS for μCT.Av and μCT.SD but not for higher order moments, as indicated by R^2_{Adj} values. Pooling the AP and LM images before calculation or averaging the results from the AP and LM views did not improve R^2_{Adj} values.

For the inferior endplate, all DTS and HRCT based average measurements were associated with μCT.Av (Table 2). SD measured from μCT (μCT.SD) was associated with SD measured from LM DTS but not from AP DTS. No significant relationship was found for higher order moments

Table 1
Results from mixed models comparing μCT to DTS and HRCT topography measurements at superior endplates. The symbol ∪ indicates that the depth measurements from AP and LM views were pooled before calculation of the distribution statistics. The symbol ā indicates that the distribution statistics from AP and LM views were averaged. For ease of comparison with DTS/HRCT averages, μCT averages are presented below each parameter in parentheses.

		μCT.Av (Av = 3.83)	μCT.SD (Av = 1.21)	μCT.Sk (Av = −0.60)	μCT.Ku (Av = 3.43)
DTS.AP	Av	2.63	0.97	−0.08	0.51
	R^2_{Adj}	0.34	0.32	0.52	0.31
	Slope	0.612	0.747	0.179	0.246
	p_{sl}	<0.0001	<0.0001	<0.03	<0.004
	Intercept	2.214	0.476	−0.576	3.293
	p_{int}	<0.0001	<0.002	<0.0001	<0.0001
DTS.LM	Av	2.79	0.95	−0.47	0.17
	R^2_{Adj}	0.21	0.27	0.51	0.31
	Slope	0.629	0.876	0.392	0.239
	p_{sl}	<0.0001	<0.0001	<0.0001	<0.002
	Intercept	2.048	0.366	−0.396	3.336
	p_{int}	<0.0001	<0.002	<0.0001	<0.0001
DTS.APULM	Av	2.71	1.05	−0.11	0.06
	R^2_{Adj}	0.30	0.20	0.53	
	Slope	0.829	0.675	0.362	
	p_{sl}	<0.0001	<0.0001	<0.0005	NS
	Intercept	1.565	0.486	−0.553	
	p_{int}	<0.0001	<0.0004	<0.0001	
DTS.APāLM	Av	2.71	0.96	−0.28	0.34
	R^2_{Adj}	0.30	0.31	0.50	0.30
	Slope	0.815	0.929	0.441	0.422
	p_{sl}	<0.0001	<0.0001	<0.0001	<0.0001
	Intercept	1.601	0.309	−0.465	3.252
	p_{int}	<0.0001	<0.02	<0.0001	<0.0001
HRCT	Av	2.89	0.88	−0.83	1.00
	R^2_{Adj}	0.37	0.19	0.57	0.40
	Slope	0.443	0.550	0.256	0.234
	p_{sl}	<0.0001	<0.0001	<0.004	<0.0009
	Intercept	2.555	0.717	−0.373	3.151
	p_{int}	<0.0001	<0.0001	<0.0003	<0.0001

Table 2
Results from mixed models comparing μCT to DTS and HRCT topography measurements at inferior endplates. The symbol ∪ indicates that the depth measurements from AP and LM views were pooled before calculation of the distribution statistics. The symbol ā indicates that the distribution statistics from AP and LM views were averaged. For ease of comparison with DTS/HRCT averages, μCT averages are presented below each parameter in parentheses.

		μCT.Av (Av = 2.96)	μCT.SD (Av = 1.89)	μCT.Sk (Av = −0.66)	μCT.Ku (Av = 2.23)
DTS.AP	Av	2.18	0.88	0.18	0.68
	R^2_{Adj}	0.14			
	Slope	0.651			
	p_{sl}	<0.0001	NS	NS	NS
	Intercept	1.624			
	p_{int}	<0.0001			
DTS.LM	Av	2.32	0.93	−0.15	0.15
	R^2_{Adj}	0.47	0.30		
	Slope	0.892	0.546		
	p_{sl}	<0.0001	<0.03	NS	NS
	Intercept	0.921	1.410		
	p_{int}	<0.0004	<0.0001		
DTS.APULM	Av	2.24	0.99	0.18	0.31
	R^2_{Adj}	0.32	0.35		
	Slope	1.112	0.925		
	p_{sl}	<0.0001	<0.0001	NS	NS
	Intercept	*0.525*	0.986		
	p_{int}	*>0.09*	<0.0002		
DTS.APāLM	Av	2.25	0.90	0.01	0.41
	R^2_{Adj}	0.34	0.28		
	Slope	1.120	0.611		
	p_{sl}	<0.0001	<0.04	NS	NS
	Intercept	*0.496*	1.366		
	p_{int}	*>0.10*	<0.0001		
HRCT	Av	2.35	0.73	−0.54	1.13
	R^2_{Adj}	0.51		0.23	
	Slope	0.636		−0.273	
	p_{sl}	<0.0001	NS	<0.02	NS
	Intercept	1.502		−0.789	
	p_{int}	<0.0001		<0.0001	

Italicized data indicates a nonsignificant intercept.

of the topography distribution for the inferior endplate. The relationship between μCT and HRCT was statistically significant for skewness; however, the slope of the regression was negative, indicating a superfluous relationship. In contrast with results for the superior endplate, calculations from μCT had stronger associations with those from LM DTS than with AP DTS. Pooling the AP and LM images before calculation or averaging the results from the AP and LM views did not improve R^2_{Adj} values.

HRCT was generally comparable to or slightly better than DTS in predicting average depth measurements and third and fourth order moments of the depth distribution but was outperformed by DTS in predicting SD of the distributions (Tables 1 and 2). The slopes of the relationships were closer to 1 (ideal relationship) for DTS than for HRCT indicating a lack of accuracy for HRCT. In addition, average and standard deviation of depth distributions were generally closer to that of μCT than were higher order statistical parameters.

Paired t-test results indicated that the mean values of average, standard deviation, and kurtosis of endplate topography distributions measured from μCT images are significantly different between superior and inferior endplates (Table 3). Average and kurtosis were significantly higher at the superior endplate, while standard deviation was lower.

All measured parameters from in vivo DTS vertebral images were within the range of in vitro data (Table 4).

4. Discussion

To our knowledge, this is the first study to demonstrate the ability to measure voxel-based topography of the entire vertebral endplate surface using clinical imaging modalities. Both tested modalities showed statistically significant correlations with μCT approaching a moderate level of correlation at the superior endplate for all measured parameters (R^2_{Adj} = 0.19–0.57, Fig. 3), including averages, variability, and higher order statistical moments. Correlation of average depths at the inferior endplate was comparable to the superior case for both DTS and HRCT (R^2_{Adj} = 0.14–0.51), while correlations became weak or nonsignificant for higher moments of the topography distribution.

DTS and HRCT have distinct advantages over each other that may help explain slightly better performance of one over the other for different measurements. Due to the blurring of the lowest and highest slices, the most lateral regions of the vertebra are excluded from analysis in the LM view, and the most anterior and posterior regions are excluded from analysis in the AP view for DTS scans (Fig. 2a). In addition, DTS has a large slice thickness (1 mm), resulting in low out of plane resolution for a given plane of view. Due to these features, DTS has poorer sampling of some regions on the endplate surface (Fig. 2b). Therefore, a slightly better performance of HRCT in measurement of average depths may be due to its sampling from a more complete space than does DTS in the axial plane. On the other hand, DTS has considerably higher resolution than HRCT in the planes of measurement (sagittal plane in LM and coronal plane in the AP scans), providing better precision for the depth values measured (Fig. 2c). Such precision would help characterize the variations in the depth distributions more accurately. This may explain

Table 3
Paired t-test results comparing statistical distribution parameters between superior and inferior endplates in μCT images. Average parameters for superior and inferior endplate are presented as ± standard deviation.

Parameter	p-Value	Superior endplate	Inferior endplate
Av (mm)	<0.0001	3.832 ± 1.367	2.956 ± 1.148
SD (mm)	<0.0001	1.205 ± 0.523	1.891 ± 0.908
Skew	0.4358	−0.598 ± 0.589	−0.664 ± 1.022
Kurt	<0.0001	3.428 ± 1.288	2.226 ± 0.898

Table 4
Preliminary comparison between endplate topography measurements made from in vivo and in vitro vertebral body images. For in vivo measurements, distribution parameters are presented for two vertebral levels from the same patient (supine/AP scan, T12, L1). Average distribution parameters are presented for 117 in vitro specimens followed by range (Min, Max). All in vivo measurements were within the range of the in vitro cohort.

	Scan type	Parameter	Av (mm)	SD (mm)	Kurt	Skew
Superior	In vivo	T12, L1	2.53, 4.10	0.94, 1.07	0.82, 0.10	0.84, −0.16
	In vitro	T10–L1 AP Av	2.64	0.97	0.49	−0.09
		(Min, Max)	(0.96, 5.57)	(0.50, 2.09)	(−1.18, 8.24)	(−1.02, 2.33)
Inferior	In vivo	T12, L1	4.10, 3.80	0.87, 0.83	1.05, 0.02	−0.92, −0.61
	In vitro	T10–L1 AP Av	2.18	0.87	0.67	0.17
		(Min, Max)	(0.64, 5.12)	(0.44, 2.51)	(−1.20, 13.06)	(−1.79, 2.73)

the correlations of SD values between DTS and μCT for the inferior endplate where the measured distances are small.

Weaker correlations in higher order distribution statistics (Tables 1–2) for both DTS and HRCT at the inferior endplate are consistent with paired t-test results which indicated that average depth from the reference plane was significantly greater at the superior endplate (Table 3). These findings are supported by in vivo radiographic endplate morphology studies which indicate that the inferior endplate is typically flatter with less concavity depth than the superior endplate [9]. Provided that DTS and HRCT have approximately 7–17 times lower measurement resolution than μCT, ability to measure differences within the topography distribution will be potentially largely affected by average depth. With a greater average depth, there are more steps available at a given voxel size to define the characteristic features contributing to changes in higher order statistical parameters.

At the superior endplate, skewness had higher correlations with μCT than kurtosis for both DTS and HRCT (Table 1). This apparent trend may be explained such that skewness, a measure of distribution asymmetry, is less sensitive to quantization of the sampling space resulting from low resolution than kurtosis, which is highly sensitive to outliers in the depth distribution (features such as high peaks in endplate morphology). Such outlying features may be missed due to infrequent sampling in coronal/sagittal directions, largely affecting kurtosis calculations. Additionally, HRCT had slightly better correlations than DTS for both skewness and kurtosis, which suggests that this trend is due to pixel spacing in coronal/sagittal planes and not due to axial pixel spacing, provided that resolution in the measurement direction is considerably less in HRCT than DTS (Fig. 2).

The current findings indicate that the topography of the endplate surface is different between the superior and inferior endplates of the same vertebra. In addition to differences in depth, we found that coronal planes (AP view, in which the endplate would be sampled with higher resolution in the transverse direction) provide more information on the superior endplate whereas sagittal planes (LM view, in which the endplate would be sampled with higher resolution in the anteroposterior direction) provide more information on the inferior endplates. This finding suggests that the nonuniformity of endplate surface is aligned in different directions for the superior endplate than for the inferior endplate. While the reasons for this may be subject of future research, this result indicates that both endplates of a vertebra should be evaluated separately during imaging studies.

Several limitations of the present study have been noted. Manual selection of threshold values produced visually acceptable segmentation (Fig. 1b–c), however methods may be refined to use image preprocessing and adaptive thresholding techniques in order to optimize and standardize characterization of the endplate surface. In addition, aside from error attributed to differences in resolution between DTS/CT and μCT, shadow artifacts inherent to limited angle tomography (objects remaining visible in slices remote to their focus plane) may contribute to error between the DTS and μCT. Although posterior elements were removed to facilitate μCT scanning in this vitro experiment, artifacts resulting from the presence of posterior elements have a minimal impact on adjacent reconstructed layers in clinical DTS scans. Preliminary data suggests that clinical DTS scans can be effectively thresholded and processed for endplate topography measurements (Fig. 4).

Although analysis of topography from statistical distributions allows general characterization of endplate surface attributes such as average depth, depth variability and presence of extreme features such as spikes and valleys, methods assessing spatial distribution and size scale of topography should be explored. As mentioned, higher order statistics are especially prone to artifacts from voids and edges. Therefore, care was taken to prepare analysis regions so as to avoid, for example, high remnants from posterior elements and improper delineation of endplate vs. cortical shell at the vertebral rim. In clinical studies, posterior elements should be similarly avoided when defining endplate analysis regions. Development of a practical, semi-automated algorithm for endplate segmentation and topography measurement in future effort could help translation to clinical assessment of vertebral endplate.

While the current study suggests that DTS can be used for characterization of endplates in vitro, the feasibility of translation to assessment of in vivo DTS images is unknown. As previously discussed, it is not possible to use microcomputed tomography as a gold standard for comparison with clinical images. The preliminary evidence that in vivo DTS images can be processed to segment vertebral endplate using the

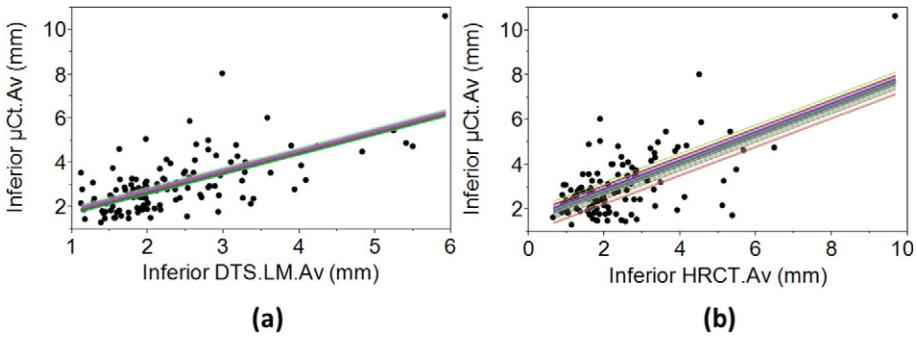

Fig. 3. Mixed regression plots of (a) inferior DTS.LM.Av vs. μCT.Av, $R^2_{Adj} = 0.47$ and (b) inferior HRCT.Av vs. μCT.Av, $R^2_{Adj} = 0.51$. The closeness of individual regression lines indicates that the effect of donor on the regression equation is small.

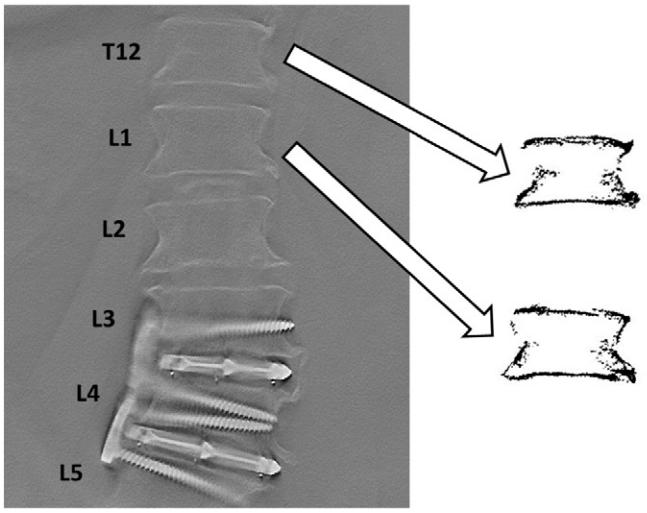

Fig. 4. Endplate topography measurements were successfully performed on two vertebral levels (T12, L1) from the same patient using clinical DTS images. Vertebral levels were selected so as to match in vitro levels and avoid implants at L3–L5. Images of T12 and L1 vertebrae were separated and thresholded (right) and depth distributions calculated using the same methods described for in vitro specimens. Measured parameters were well within the range of in vitro specimens (Table 4).

same protocols as in vitro specimens, together with relative agreement of the calculated values (Table 4), suggests that in vivo endplate topography measurement is feasible. Although the accuracy of the measured variables needs further improvement, the relationships found in the current study might be useful on a comparative basis.

In conclusion, DTS and HRCT performed comparably for measurement of average distances, both having moderate levels of correlations with μCT. DTS was able to capture variations in the endplate topography to a slightly better extent than HRCT. Based on these findings and the higher speed and lower radiation cost of DTS than HRCT, DTS appears preferable for endplate measurements. It remains to be seen the extent to which DTS based assessment of endplate geometry will help elucidate the degenerative processes underlying the degradation of spinal tissue qualities in a clinical setting.

Acknowledgments

This project was supported, in part, by the National Institutes of Health under Grant Number AR059329. Its contents are solely the responsibility of the authors and do not necessarily represent the official views of the NIH. David Hovis, Ph.D. of Case Western Reserve University Swagelok Center for Surface Analysis of Materials provided a modified version of the TopoJ plugin for ImageJ. Human tissue used in the presented work was provided by NDRI (National Disease Research Interchange) and Platinum Training.

References

[1] S.K. Eswaran, A. Gupta, T.M. Keaveny, Locations of bone tissue at high risk of initial failure during compressive loading of the human vertebral body, Bone 41 (2007) 733–739.
[2] P.A. Hulme, S.K. Boyd, S.J. Ferguson, Regional variation in vertebral bone morphology and its contribution to vertebral fracture strength, Bone 41 (2007) 946–957.
[3] N.A. Langrana, S.P. Kale, W.T. Edwards, C.K. Lee, K.J. Kopacz, Measurement and analyses of the effects of adjacent end plate curvatures on vertebral stresses, Spine J. 6 (2006) 267–278.
[4] I.P. Pappou, F.P. Cammisa, F.P. Girardi, Correlation of end plate shape on MRI and disc degeneration in surgically treated patients with degenerative disc disease and herniated nucleus pulposus, Spine J. 7 (2007) 32–38.
[5] S. Roberts, I.W. McCall, J. Menage, M.J. Haddaway, S.M. Eisenstein, Does the thickness of the vertebral subchondral bone reflect the composition of the intervertebral disc? Eur. Spine J. 6 (1997) 385–389.
[6] S. Nekkanty, J. Yerramshetty, D.G. Kim, R. Zauel, E. Johnson, D.D. Cody, Y.N. Yeni, Stiffness of the endplate boundary layer and endplate surface topography are associated with brittleness of human whole vertebral bodies, Bone 47 (2010) 783–789.
[7] A. Noshchenko, A. Plaseied, V.V. Patel, E. Burger, T. Baldini, L. Yun, Correlation of vertebral strength topography with 3-dimensional computed tomographic structure, Spine 38 (2013) 339–349.
[8] P. Lakshmanan, B. Purushothaman, V. Dvorak, W. Schratt, S. Thambiraj, M. Boszczyk, Sagittal endplate morphology of the lower lumbar spine, Eur. Spine J. 21 (Suppl. 2) (2012) S160–S164.
[9] Y. Wang, M.C. Battie, T. Videman, A morphological study of lumbar vertebral endplates: radiographic, visual and digital measurements, Eur. Spine J. 21 (2012) 2316–2323.
[10] E.B. van der Houwen, P. Baron, A.G. Veldhuizen, J.G. Burgerhof, P.M. van Ooijen, G.J. Verkerke, Geometry of the intervertebral volume and vertebral endplates of the human spine, Ann. Biomed. Eng. 38 (2010) 33–40.
[11] B.G. Ziedses des Plantes, Seriescopy, Een Rontgenographische method welke het mogelijk maakt achtereenvolgens een oneindig aantal evenwijdige vlakken van het te onderzoeken voorwerp afzonderlijk te bechouwen (Seriescopy, a Roentgenographic method which allows an infinite number of successive parallel planes of the test object to be considered separately) (English translation), Ned. Tijdschr. Geneeskd. 51 (1935) 5852–5856.
[12] J.B. Garrison, D.G. Grant, W.H. Guier, R.J. Johns, Three dimensional roentgenography, Am. J. Roentgenol. Radium Ther. Nucl. Med. 105 (1969) 903–908.
[13] E.E. Hoefer, H. Grimmert, B. Kieslich, Computer-controlled synthesis of tomograms by means of a TV storage tube, IEEE Trans. Biomed. Eng. 21 (1974) 243–244.
[14] E.C. Lasser, N.A. Baily, R.L. Crepeau, A fluoroplanigraphy system for rapid presentation of single plane body sections, Am. J. Roentgenol. Radium Ther. Nucl. Med. 113 (1971) 574–577.
[15] D.J. Godfrey, A. Rader, J.T. Dobbins Iii, Practical strategies for the clinical implementation of matrix inversion tomosynthesis (MITS), 2003 379–390.
[16] R.E. Gazaille III, M.J. Flynn, W. Page III, S. Finley, M. van Holsbeeck, Technical innovation: digital tomosynthesis of the hip following intra-articular administration of contrast, Skelet. Radiol. 40 (2011) 1467–1471.
[17] M.J. Flynn, R. McGee, J. Blechinger, Spatial resolution of X-ray tomosynthesis in relation to computed tomography for coronal/sagittal images of the knee, 2007 SPIE Conference, Medical Imaging. San Diego, CA, 2007.
[18] Y. Zhang, L. Xiang, W.P. Segars, E. Samei, Comparative dosimetry of radiography, tomosynthesis, and CT for chest imaging across 59 adult patients, 2013 SPIE Conference, Medical Imaging. Lake Buena Vista, FL, 2013.
[19] M.M. Thornton, M.J. Flynn, Measurement of the spatial resolution of a clinical volumetric computed tomography scanner using a sphere phantom, 2006 SPIE Conference, Medical Imaging. San Diego, CA 2006, p. 61421Z (p. 61421Z-61421Z-10).
[20] D.A. Reimann, S.M. Hames, M.J. Flynn, D.P. Fyhrie, A cone beam computed tomography system for true 3D imaging of specimens, Appl. Radiat. Isot. 48 (1997) 1433–1436.
[21] R. Zauel, D.P. Fyhrie, Y.N. Yeni, Segmentation algorithm with improved connectivity for accurate 3D representation of microcomputed tomographic images of human vertebral bodies, 51st Annual Meeting of the Orthopaedic Research Society. Washington, D.C. 2005, p. 1260.
[22] H.R. Buie, G.M. Campbell, R.J. Klinck, J.A. MacNeil, S.K. Boyd, Automatic segmentation of cortical and trabecular compartments based on a dual threshold technique for in vivo micro-CT bone analysis, Bone 41 (2007) 505–515.
[23] W.S. Rasband, ImageJ, U. S. National Institutes of Health, 1997–2014.
[24] ASME, Surface Texture: Surface Roughness, Waviness and Lay, American Society of Mechanical Engineers, New York, 2003.
[25] W.Z. Wang, H. Chen, Y.Z. Hu, H. Wang, Effect of surface roughness parameters on mixed lubrication characteristics, Tribol. Int. 39 (2006) 522–527.
[26] M. Sedlacek, L.M.S. Vilhena, B. Podgornik, J. Vizintin, Surface topography modelling for reduced friction, Strojniski Vestn. J. Mech. Eng. 57 (2011) 674–680.